Correction: 20 November 2015

www.sciencemag.org/cgi/content/full/science.aad1015/DC1

# Supplementary Materials for

## Efficient and stable large-area perovskite solar cells with inorganic charge extraction layers

Wei Chen,* Yongzhen Wu,* Youfeng Yue, Jian Liu, Wenjun Zhang, Xudong Yang, Han Chen, Enbing Bi, Islam Ashraful, Michael Grätzel,† Liyuan Han†

*These authors contributed equally to this work.
†Corresponding author. E-mail: michael.graetzel@epfl.ch (M.G.); han.liyuan@nims.go.jp (L.H.)

Published 29 October 2015 on *Science* Express
DOI: 10.1126/science.aad1015

**This PDF file includes:**



**Correction:** Reference 34 was mistakenly listed as X. F. Chen *et al.*, *Int. J. Clin. Exp. Med.* **8**, 5044–5054 (2015). The correct reference 34 is W. Chen *et al.*, *Energy Environ. Sci.* **8**, 629–640 (2015). The PDF has been corrected.

## Materials and Methods

Materials

All the chemicals were used as received, including $PbI_2$ (99%, Sigma–Aldrich), $CH_3NH_3I$ (> 98%, Tokyo Chemical Industry Co., Japan), Titanium isopropoxide (99.999%, Sigma–Aldrich), niobium ethoxide (99.95%, Sigma–Aldrich), nickel acetylacetonate (95%, Sigma–Aldrich), $PC_{61}BM$ (99.5%, Lumtec Co., Taiwan). Magnesium acetatetetrahydrate (99%), lithium acetate (99%) and super dehydrated solvents of dimethylsulfoxide (DMSO), toluene, chlorobenzol, acetonitrile, methanol and ethanol, were all purchased from Wako Co., Japan.

Thin Film and Solar Cell Fabrication

FTO glasses (Nippon Sheet Glass Co., Japan) with a sheet resistance of 8–10 $ohm^{-2}$ and an optical transmission of greater than 80% in the visible range were used. After thoroughly washing with cleaning fluid, deionized water, ethanol and acetone, the clean FTO glasses were placed on a hotplate at the temperature of 500 °C. 30 ml of an acetonitrile/ethanol (with 95: 5 volume ratio) solution of nickel acetylacetonate (or with 15 mol% magnesium acetatetetrahydrate and 5 mol% lithium acetate) was sprayed within 10 min by an air nozzle (with 0.2 mm caliber) onto the hot FTO glasses at a distance of about 20 cm above. The total metal ion concentration was set at 0.02 mol $L^{-1}$. After spraying, the film was further treated at 500 °C for another 20 min to promote NiO crystallization. NiO film thickness could be tuned from 10 to 40 nm by varying the solution volume from 15 to 60 ml. After cooling, the NiO coated FTO glasses were transferred quickly to the $N_2$ filled glove box for $MAPbI_3$ perovskite layer deposition. The method for perovskite layer deposition was modified slightly from previous report(*6*): first, a 80 μl 1.45 M DMSO solution of $PbI_2$/MAI mixture was spread onto 70 °C FTO glass (2.4× 2.4 $cm^2$ in size); then, the spin–coater was started at a rotation speed of 1000 rpm for 10 seconds and 5000 rpm for another 30 seconds. 800 μl toluene was drop–casted quickly 10 seconds after the 5000 rpm spin–coating started. The perovskite films were then heated at 100 °C on a hotplate for 10 min. After cooling, a chlorobenzol solution of PCBM (20 mg $ml^{-1}$) was spin–coated on top of the perovskite film at the rotation speed of 1000 rpm for 30 seconds. Subsequently, 100 μl $TiO_x$ precursor solution, containing titanium isopropoxide (or with 5 mol% niobium ethoxide) diluted in methanol with volume ratio of 1/200–1/600, was drop–casted slowly onto the surface of PCBM layer at the rotation speed of 6000 rpm. After the film was dried at 70 °C for 10 minutes, 150 μl $H_2O$/methanol mixed solution (with 1: 99 volume ratio) was drop–casted slowly at the rotation speed of 6000 rpm for 30 seconds, to promote hydrolysis of previously deposited titanium isopropoxide. The film was then dried at 70 °C for 30 min to promote condensation of titanium hydroxide, leading to $TiO_x$ formation. At last, one batch of films were transferred to the evaporator chamber, 100 nm thick Ag contacts were deposited under high vacuum (< $3\times10^{-4}$ Pa). For solar cell sealing, a cavity glass with UV glue on the edges was sandwiched with the front FTO glass with the active films in–between. After exposure to 300 W UV light for 15 seconds, the sealing process was terminated. All of these processes were done in glove box.

Characterizations

SEM images were obtained by using a JSM–6500F field–emission scanning electron microscope. TEM observations were carried out on a JEM–ARM200F transmission electron microscope. For cross sectional observation of NiO films, the samples were prepared by using a FIB cutting technique. Electric conductivity of the charge extraction films (NiO based films on FTO glass, and $TiO_x$ based films on PCBM covered ITO glass) was investigated by using the contact–current mode of a scanning probe microscope (SPM; JEOL JSPM–5200). The XPS and UPS measurements were performed in a Kratos Ultra Spectrometer (AXIS–ULTRA DLD–600W) using monochromatized Al Kα X–ray photons (h$\nu$ = 1486.6 eV for XPS) and a HeI (21.2 eV for UPS) discharge lamp. A Ecopia HMS 5500 Hall system was applied to measure the room–temperature conductivity and Hall coefficient (*RH*) by using the van der Pauw method with a magnetic field strength of 0.550 T, and the carrier concentration (*n*) was calculated according to the equations: $|RH| = 1/ne$, where *e* is the electrical charge of the electron. The UV–Vis spectra were measured on a Shimadzu UV/Vis 3600 spectrophotometer with an integrating sphere. The thickness of NiO based films was observed and measured by SEM. The thickness of $TiO_x$ based films (on top of PCBM covered ITO glasses) was measured by a Surfcom 1400A surface profiler (Tokyo Seimitsu Co. Ltd.) deducting the thickness of PCBM underlayers.

The current–voltage characteristics were measured using a black metal mask with an aperture area of 0.09 or 1.02 $cm^2$ under standard air mass 1.5 sunlight (100 mW $cm^{-2}$, WXS–155S–10: Wacom Denso Co., Japan). Monochromatic incident photon–to–current conversion efficiency (IPCE) spectra were measured with a monochromatic incident light of $1 \times 10^{16}$ photons $cm^{-2}$ in director current mode (CEP–2000BX, Bunko–Keiki). The light soaking stability was tested in a solar cell light resistance test system (Model BIR–50, Bunkoh–Keiki Co., LTD) equipped with a Class AAA solar simulator; <420 nm UV light was cut off with an optical filter. The time–resolved photoluminescence characterizations were done on an Edinburg FLS 920 (Edinburg90 Co. LTD), and the excitation was provided by a picosecond pulsed light emitting diode (EPLED-445) at the wavelength of 445 nm with pulse width of 95.3 ps. Transient photovoltage/photocurrent decay measurements were done on a home–made system. A white light bias on the sample was generated from an array of diodes. Red light pulse diodes (0.05 s square pulse width, 100 ns rise and fall time) controlled by a fast solid–state switch were used as the perturbation source. The transient photocurrent was measured using 20 ohm external series resistance to operate the device in short circuit. Similarly, transient photovoltage was measured using 1 MΩ external series resistance to operate the device in open circuit. The voltage dynamics on the resistors were recorded on a digital oscilloscope (Tektronix MDO3032). The perturbation red light source was set to a suitably low level to the white diodes array with light intensity equivalent to 100 mW $cm^{-2}$ of a standard solar simulator.

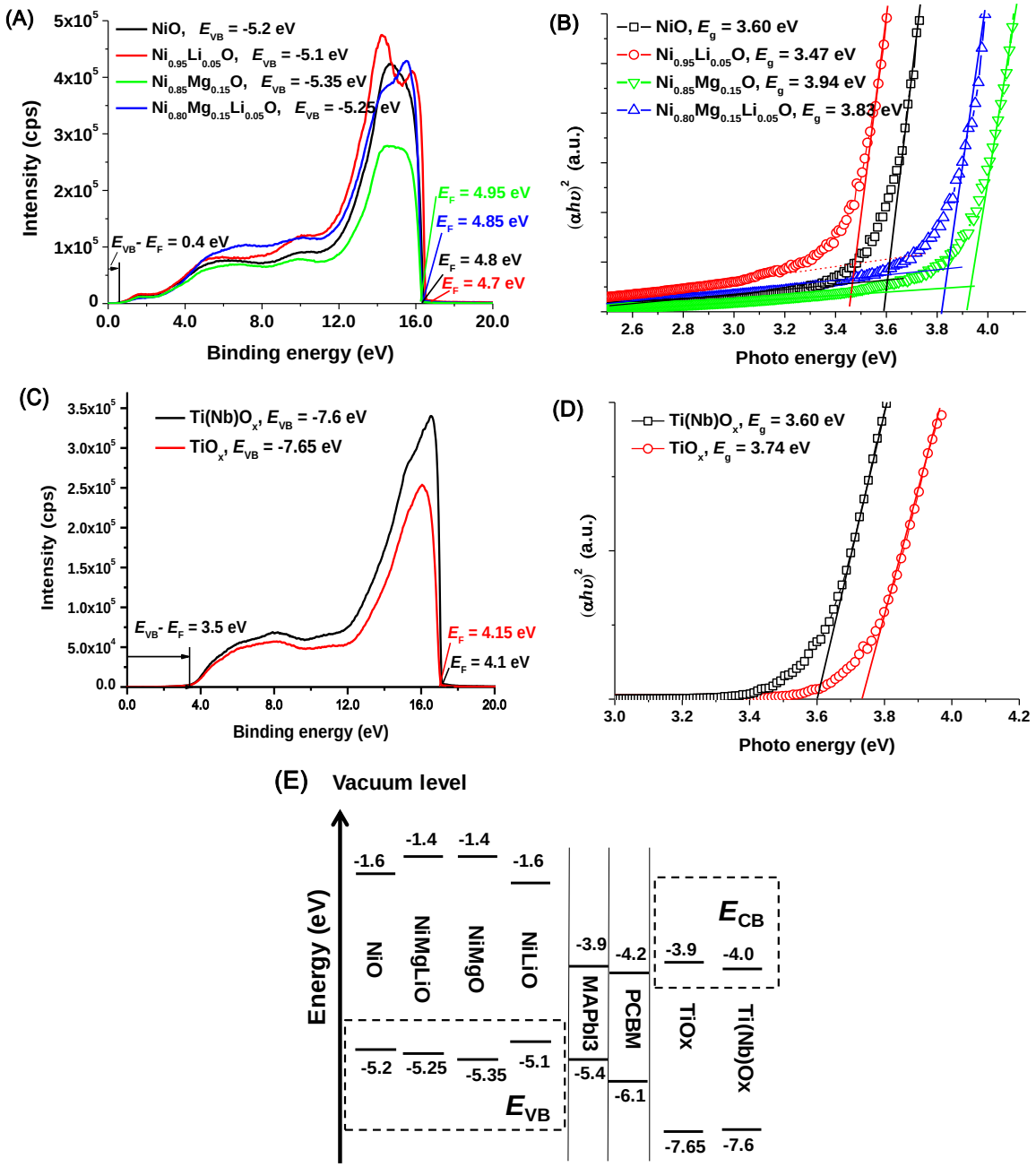


**Fig. S1.**

(A) UPS and (B) UV–Vis spectra of the NiO based charge extraction layers with and without doping. NiMgLiO, NiMgO and NiLiO represent $Mg_{0.15}Li_{0.05}Ni_{0.80}O$, $Mg_{0.15}Ni_{0.85}O$ and $Li_{0.05}Ni_{0.95}O$, respectively. (C) UPS and (D) UV–Vis spectra of the $TiO_x$ based charge extraction layers with and without doping. (E) Summary on the calculated band edge positions of the charge extraction layers with respect to $MAPbI_3$ and PCBM.

The work function, or Fermi level ($E_F$) of the charge carrier extraction layers are obtained by subtracting the binding energies of the secondary electron cutoffs (in the range of 16–18 eV) from the excitation energy (21.2 eV) of HeI UPS spectra. The energy

difference between the valance band maximum ($E_{VB}$) and $E_F$ was derived from the low binding energy tails (in the range below 4 eV). Conduction band ($E_{CB}$) edge values were obtained by adding the optical band gaps ($E_g$) to $E_{VB}$.

Both NiO and MgO exhibit rock–salt structures with a small (0.8%) lattice mismatch. The lattice constant for NiO and MgO is 4.177 Å and 4.213 Å, respectively. Therefore, solid solution of $Ni_xMg_{1-x}O$ (x = 0–1) could be obtained as reported in the literatures. At the same time, according to Vegard's law, the band gaps of the $Ni_xMg_{1-x}O$ alloys could be continuously tuned by varying "x"(*38*). The value of $Ni_{0.85}Mg_{0.15}O$ determined from this work with a wider band gap and about 0.15 eV deeper valance band are consistent with the literature (*37*).

$Ni_{1-x}Li_xO$ also has very high doping tolerance. The NiLiO alloy with "x" value up to 0.25 has been reported without crystal structure change (*48*). Suitable Li doping could greatly enhance the conductivity of NiO, allowing $Ni_{1-x}Li_xO$ to be a candidate for a p–type TCO material. The optimal "x" value for the highest conductivity as reported in the literatures is around 3–10% (*49*). In this work, x = 5% was selected as the target composition, in order to prevent too much change on $E_{VB}$ and $E_g$.

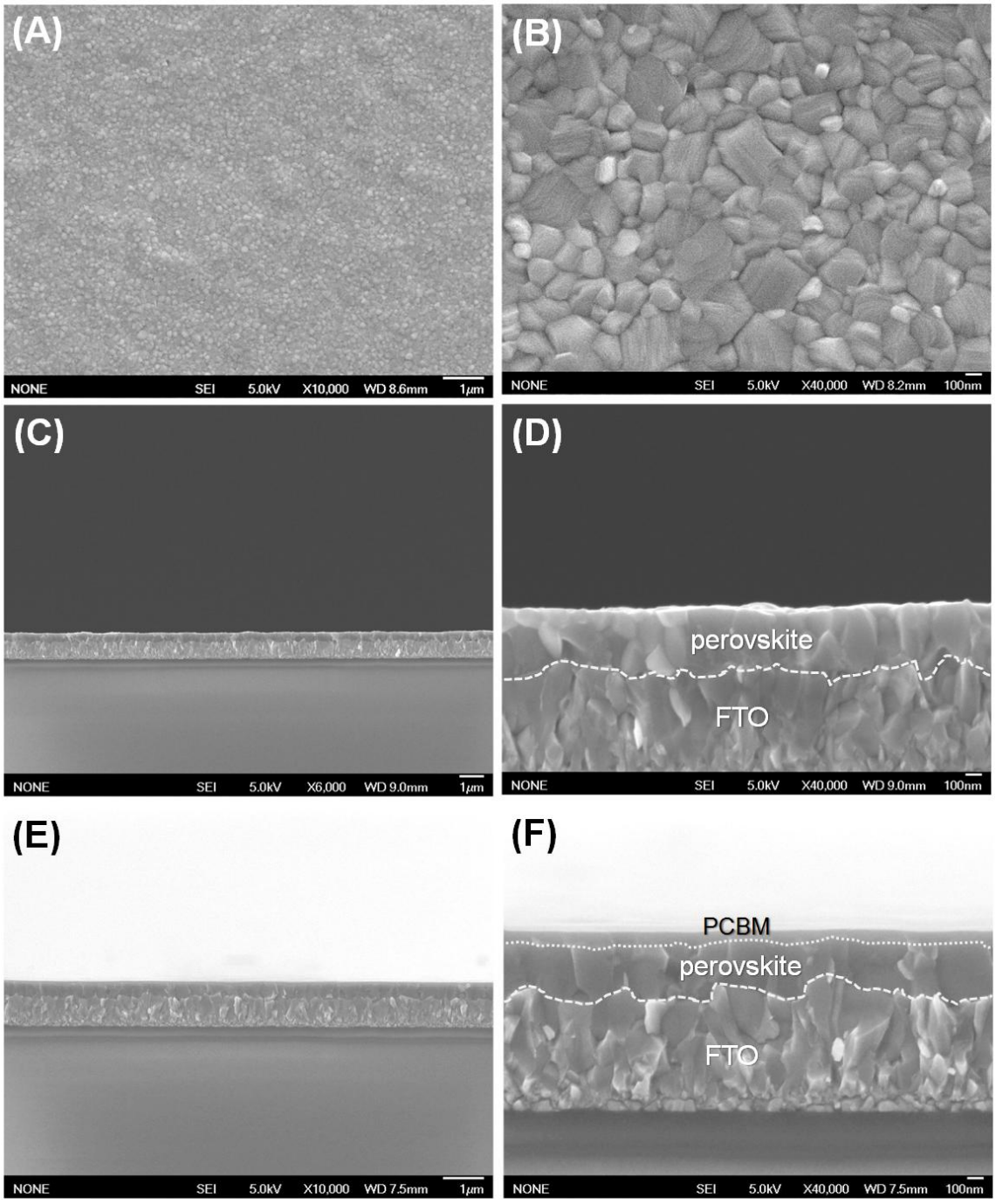


**Fig. S2**

(**A**–**B**) Top view and (**C**–**D**) cross–sectional view of SEM images of $MAPbI_3$ film on FTO glass. The average crystal size is about 300 nm and average film thickness is about 300 nm. Therefore, the number of grain boundaries within the cross–sectional charge transport paths is small. (**E**–**F**) cross–section view SEM images of $MAPbI_3$ films coated with PCBM layer. The average thickness of PCBM is 80 nm. The surface roughness becomes lower after PCBM coating.

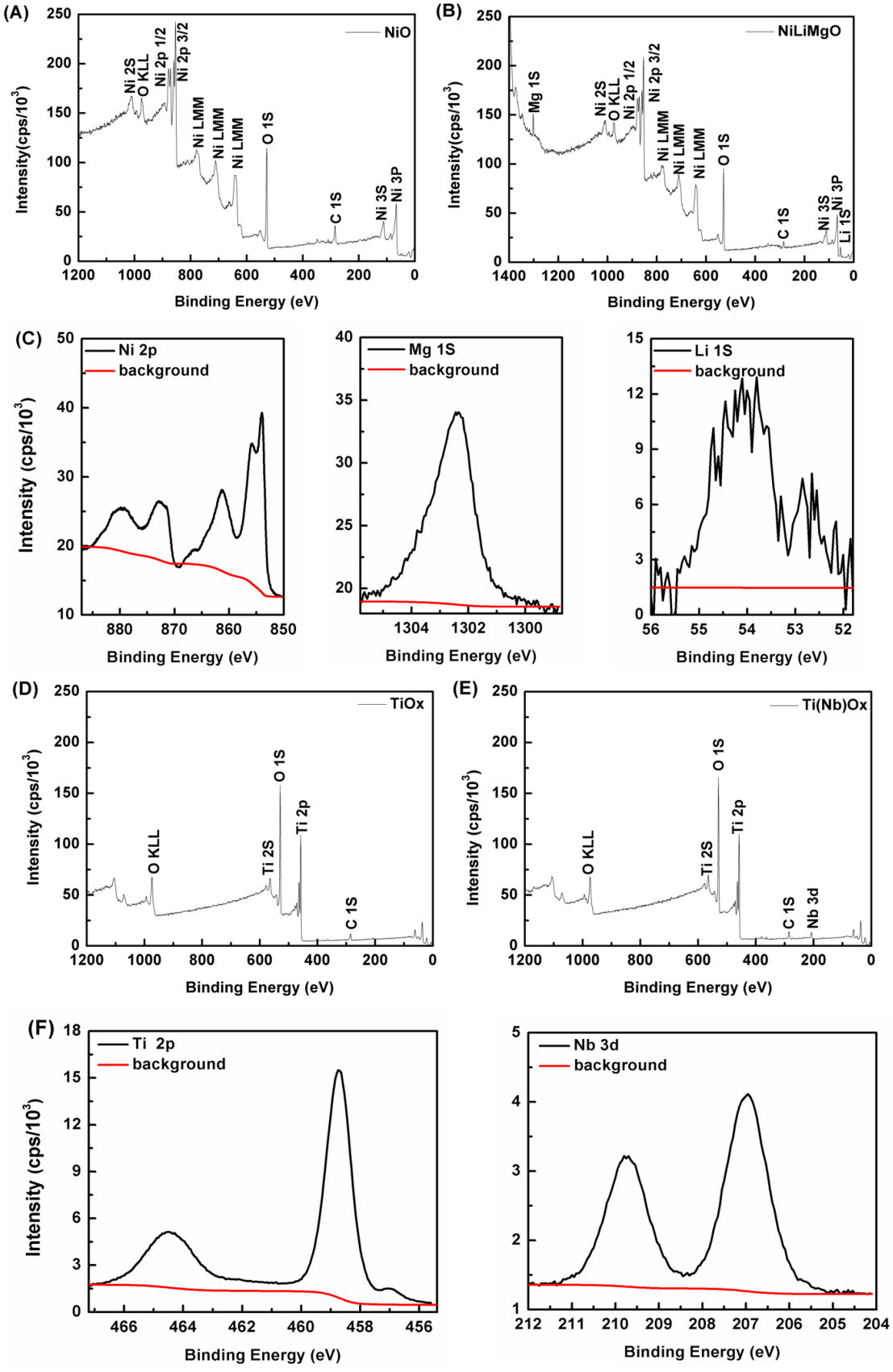
(A)
NiO
Ni 2S
O KLL
Ni 2p 1/2
Ni 2p 3/2
Ni LMM
Ni LMM
Ni LMM
O 1S
C 1S
Ni 3S
Ni 3P
Intensity(cps/10^3)
Binding Energy (eV)
(B)
NiLiMgO
Mg 1S
Ni 2S
O KLL
Ni 2p 1/2
Ni 2p 3/2
Ni LMM
Ni LMM
Ni LMM
O 1S
C 1S
Ni 3S
Ni 3P
Li 1S
Intensity(cps/10^3)
Binding Energy (eV)
(C)
Ni 2p
background
Intensity (cps/10^3)
Binding Energy (eV)
Mg 1S
background
Binding Energy (eV)
Li 1S
background
Binding Energy (eV)
(D)
TiOx
O KLL
Ti 2S
O 1S
Ti 2p
C 1S
Intensity (cps/10^3)
Binding Energy (eV)
(E)
Ti(Nb)Ox
O KLL
Ti 2S
O 1S
Ti 2p
C 1S
Nb 3d
Intensity (cps/10^3)
Binding Energy (eV)
(F)
Ti 2p
background
Intensity (cps/10^3)
Binding Energy (eV)
Nb 3d
background
Binding Energy (eV)

**Fig. S3**

Wide survey XPS spectra of (**A**) NiO film, (**B**) NiMgLiO film, with atomic ratios of Ni: Mg: Li = 81.2: 14.5: 4.3 calculated by the relative peak area/ sensitivity factor from the narrow scan data in (**C**); Wide survey XPS spectra of (**D**) $TiO_x$ film, (**E**) $Ti(Nb)O_x$, with atomic ratio of Ti: Nb = 94.7: 5.3 calculated by the relative peak area/ sensitivity factor from the narrow scan data in (**F**).

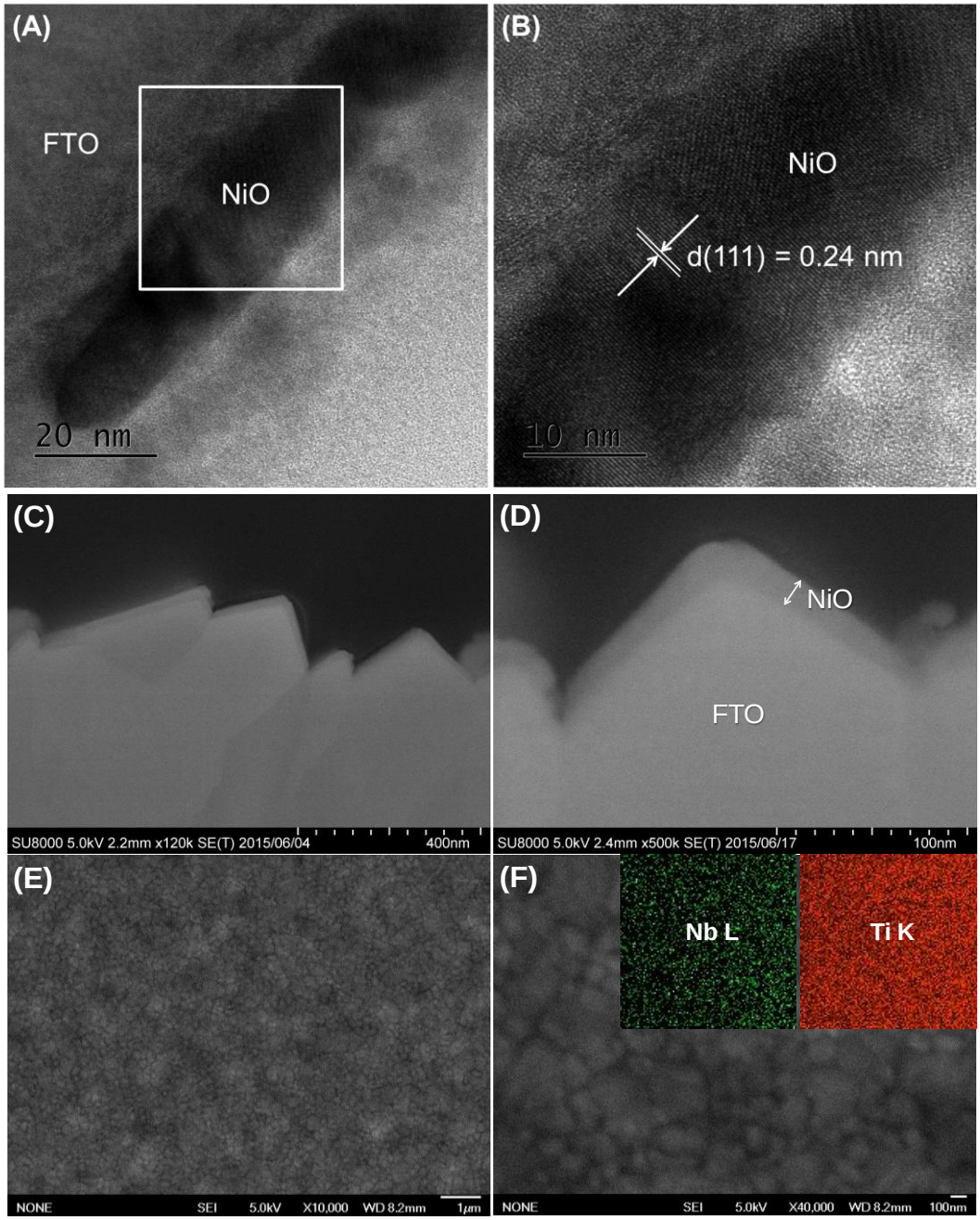


**Fig. S4**

Cross–section view of (**A**–**B**) TEM images and (**C**–**D**) backscattered electron (SE(T)) SEM images of 20 nm thick NiO films on FTO glasses; the cross sectional samples were prepared by the special FIB cutting technique; from high resolution TEM image in (**B**), the crystalline lattice owing to NiO could be identified; the apparent contrast between FTO and NiO coatings could be clearly identified from the SEM images, demonstrating a highly compact and uniform overage of NiO on FTO. (**E**–**F**) top view SEM images of $Ti(Nb)O_x$ coated $MAPbI_3$/PCBM films on FTO glasses. The insets in (**F**) are EDX mapping results at the same SEM observed region, reflecting the uniform coating morphology and elemental distribution of the $Ti(Nb)O_x$ layer.

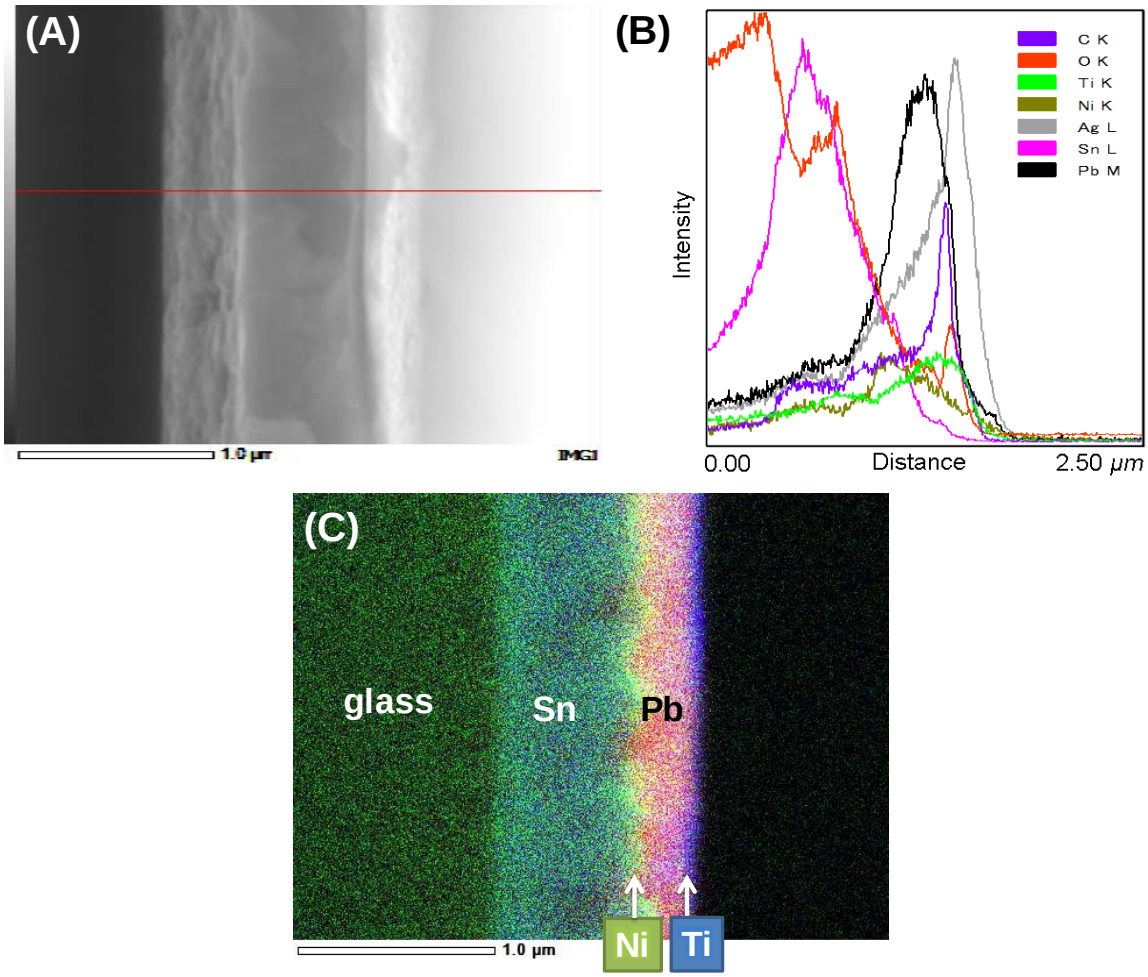


**Fig. S5**

SEM–EDX analysis results of a complete solar cell, demonstrating the layer by layer structure and NiMgLiO/Ti(Nb)$O_x$ based charge carrier extraction layers that are present in the correct locations. (**A**) SEM image for EDX analysis; (**B**) EDX linear–scan analysis result: the peak of Pb is sandwiched between Ni and Ti, and the peak of Ti is sandwiched between C and Ag; (**C**) the overlaid EDX mapping results of Sn (from FTO), Ni (from NiMgLiO), Pb (from perovskite) and Ti (from Ti(Nb)$O_x$) elements.

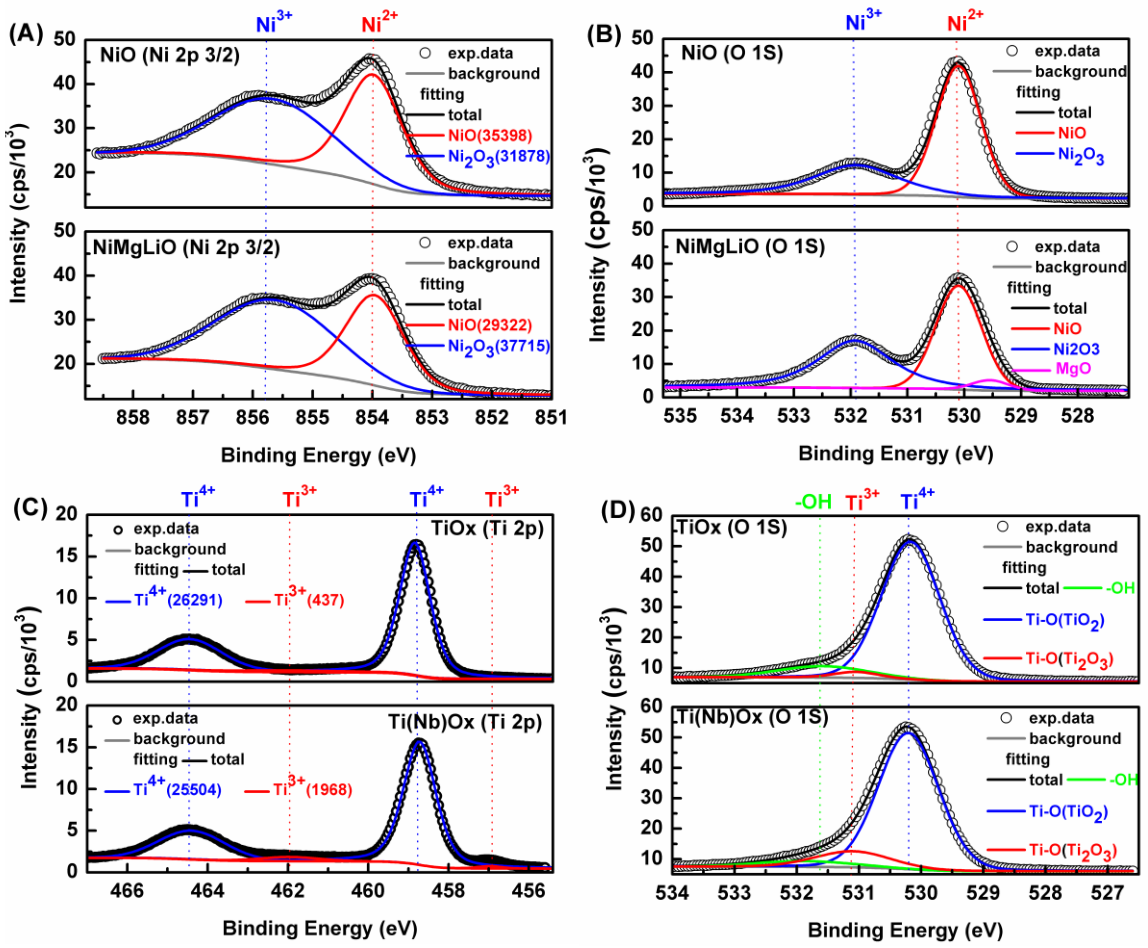


**Fig. S6**

Deconvolution of (**A**) Ni 2p3/2 and (**B**) O1s XPS spectra of NiO/NiMgLiO films, and (**C**) Ti 2p and (**D**) O 1s XPS spectra of $TiO_x$/Ti(Nb)$O_x$ films. The integrated areas of the fitted peaks are denoted in the corresponding brackets showing that the relative content of $Ni^{3+}/Ni^{2+}$ and $Ti^{3+}/Ti^{4+}$ are increased upon doping.

(A)

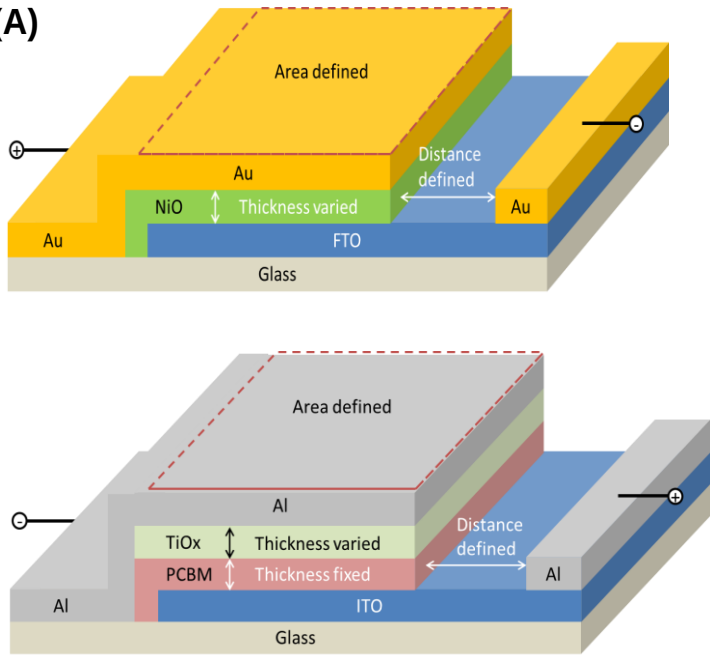


(B)

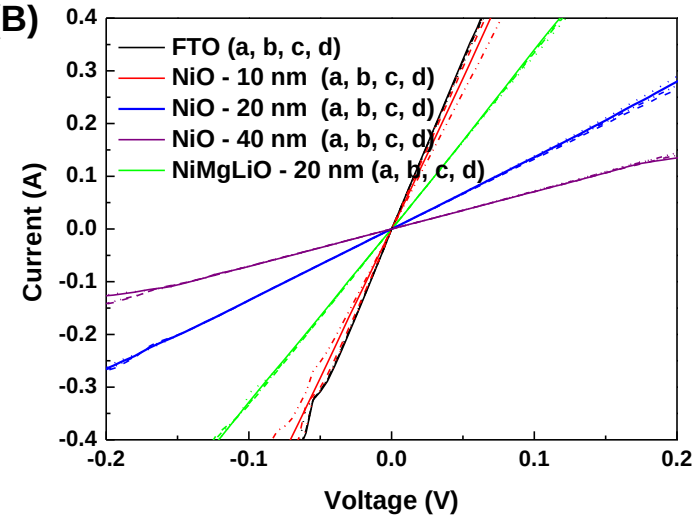


(C)

| P-type hole extraction layers' resistivity ($10^{-1}$ ohm) | | | | |
|---|---|---|---|---|
| | FTO | NiO - 10 nm | NiO - 20 nm | NiO - 40 nm |
| Sample-a | 1.80 | 1.83 | 7.35 | 13.91 |
| Sample-b | 1.82 | 1.84 | 7.39 | 14.03 |
| Sample-c | 1.76 | 1.79 | 7.23 | 13.98 |
| Sample-d | 1.81 | 1.98 | 7.44 | 14.07 |

(D)

| N-type electron extraction layers' resistivity (ohm) | | | | |
|---|---|---|---|---|
| | PCBM | TiOx - 5 nm | TiOx - 10 nm | TiOx - 20 nm |
| Sample-a | 0.23 | 0.24 | 1.11 | 2.03 |
| Sample-b | 0.23 | 0.29 | 1.16 | 2.05 |
| Sample-c | 0.23 | 0.25 | 1.15 | 2.10 |
| Sample-d | 0.24 | 0.31 | 1.19 | 2.07 |

**Fig. S7**

Electrical measurement to check the pin–hole free morphology of the charge extraction layers. (**A**) The design patterns for the measurement: for NiO films, a high work function Au contact was used; while for $TiO_x$ films, the low work function Al contact was used, a PCBM under–layer was used to simulate the situation in real solar cells. (**B**) The *I–V* curves of different p–type film samples obtained by linear sweep voltammetry. (**C**) The calculated resistances of NiO films with different thicknesses from the slopes of the *I–V* curves for the parallel 4 samples on one substrate. (**D**) The calculated resistances of $TiO_x$ films with different thicknesses from the slopes of the *I–V* curves measured based on the design in **(A)**.

The increased resistance in comparison to bare FTO or bare PCBM are associated with charge extraction layers with different thickness. For the NiO–10 nm and $TiO_x$–5nm films, their increased resistances are not proportional to their thickness, which is due to the presence of many pinholes inside the films leading to many short–cuts for charge leakage. This numerically electrical method is effective to judge the pin–hole density inside the blocking layers; the measurement results are consistent with the trend of the corresponding solar cells' *J–V* curves.

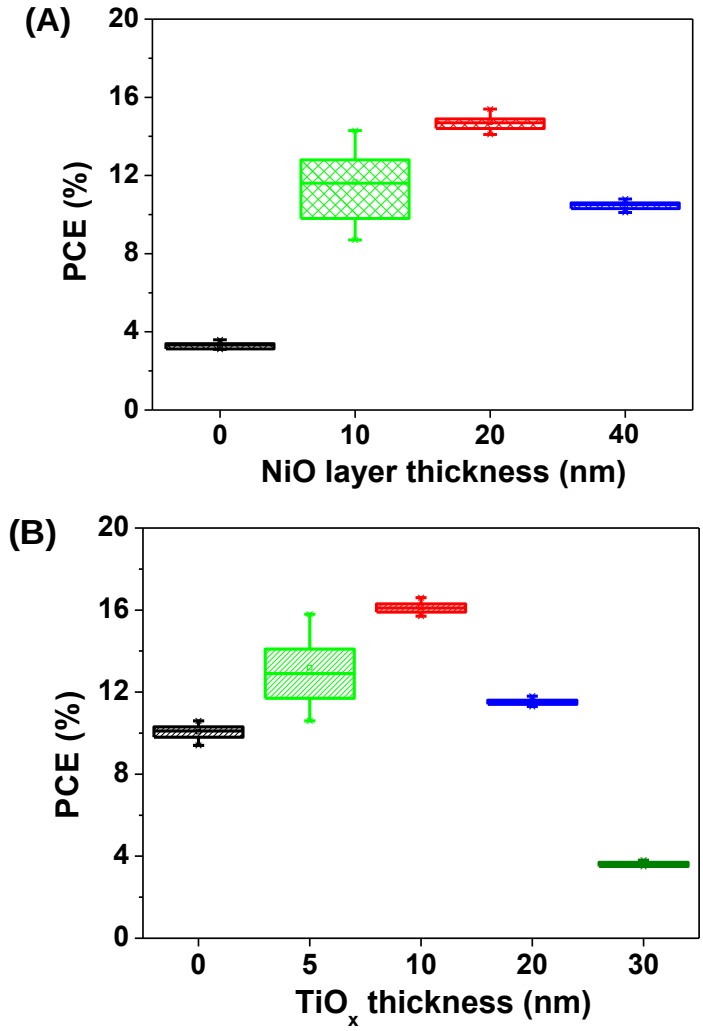


**Fig. S8**

Statistics on performance variations of the solar cells (aperture area: 0.09 $cm^2$) based on the charge extraction layers with controlled thicknesses (20 cells for each condition). (**A**) The undoped NiO layer thickness = 0, 10, 20, 40 nm, with fixed Ti(Nb)$O_x$ layer thickness of 10 nm; (**B**) The undoped $TiO_x$ layer thickness = 0, 5, 10, 20, 30 nm with fixed NiMgLiO layer thickness of 20 nm.

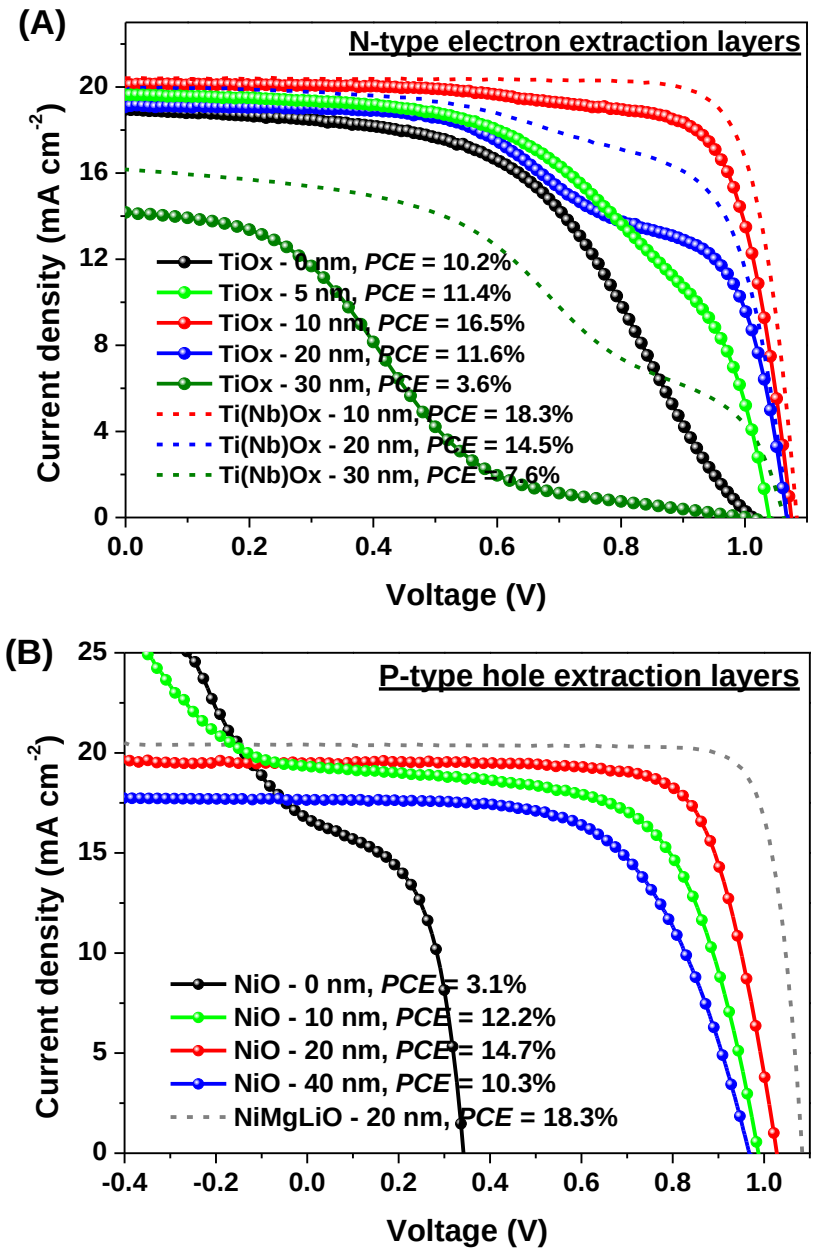


**Fig. S9**

Typical *J*–*V* curves of the solar cells (0.09 $cm^2$) based on the charge carrier extraction layers with controlled thickness. (**A**) The thicknesses of $TiO_x$ films varied from 0, 5, 10, 20 to 30 nm and $Ti(Nb)O_x$ films varied from 10, 20 to 30 nm, with fixed 20 nm NiMgLiO. The largely decreased current at the high voltage range of 0.7–1.0 V is due to poor electron extraction by the $TiO_x$ layer: for 5 nm $TiO_x$ film, the decreased current is due to insufficient coverage; while for $TiO_x$ films thicker than 10 nm, largely increased bulk resistance of $TiO_x$ becomes a hindering factor for electron transport; with the same thickness of 10, 20 and 30 nm, the doped $Ti(Nb)O_x$ films performed better than the undoped $TiO_x$ films due to improved electron extraction, meanwhile the thickness increase of $Ti(Nb)O_x$ films resulted in smaller performance decline. (**B**) The thicknesses

of NiO films varied from 0, 10, 20 to 40 nm and NiMgLiO film of 20 nm, with fixed 10 nm Ti(Nb)$O_x$. The largely increased currents at the bias region NiO–0 nm and NiO–10 nm samples are due to the short–cuts between perovskite and FTO, which is consistent with the $TiO_2$ based PSC with porous blocking layer reported in (*50*).

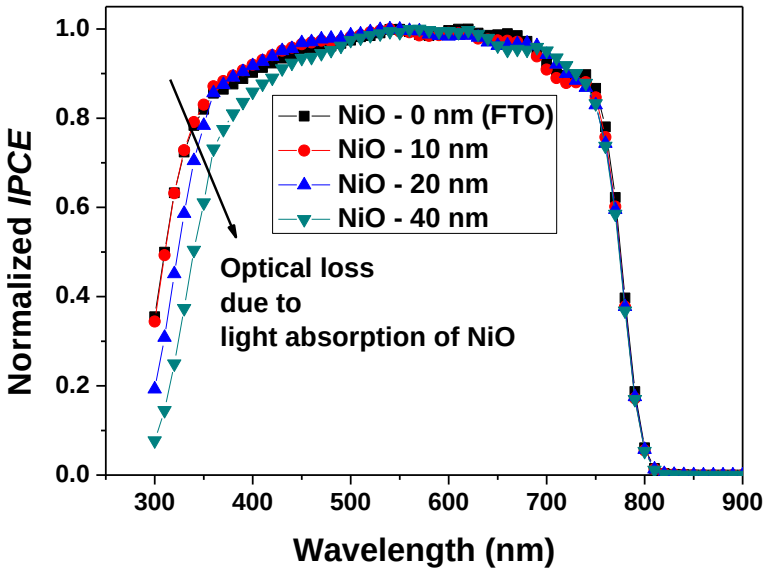


**Fig. S10**

Normalized *IPCE* spectra of the solar cells based on NiO charge carrier extraction layers with different thicknesses. Optical loss in the short wavelength region (<500 nm) increases as the NiO film thickness increasing, leading to lower *IPCE* in that region.

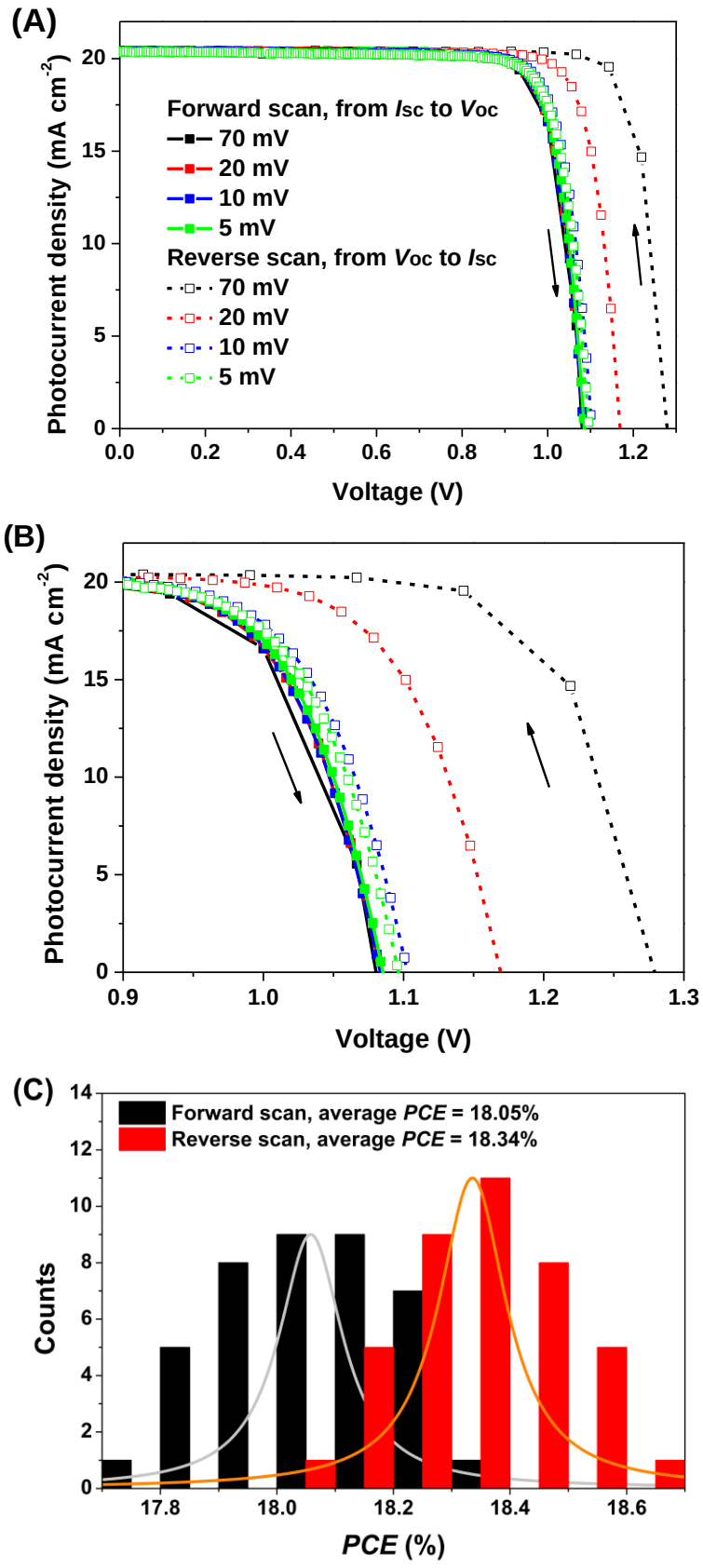
(A)
Photocurrent density (mA cm-2)
Voltage (V)
Forward scan, from Isc to Voc
70 mV
20 mV
10 mV
5 mV
Reverse scan, from Voc to Isc
70 mV
20 mV
10 mV
5 mV
(B)
Photocurrent density (mA cm-2)
Voltage (V)
(C)
Forward scan, average PCE = 18.05%
Reverse scan, average PCE = 18.34%
Counts
PCE (%)

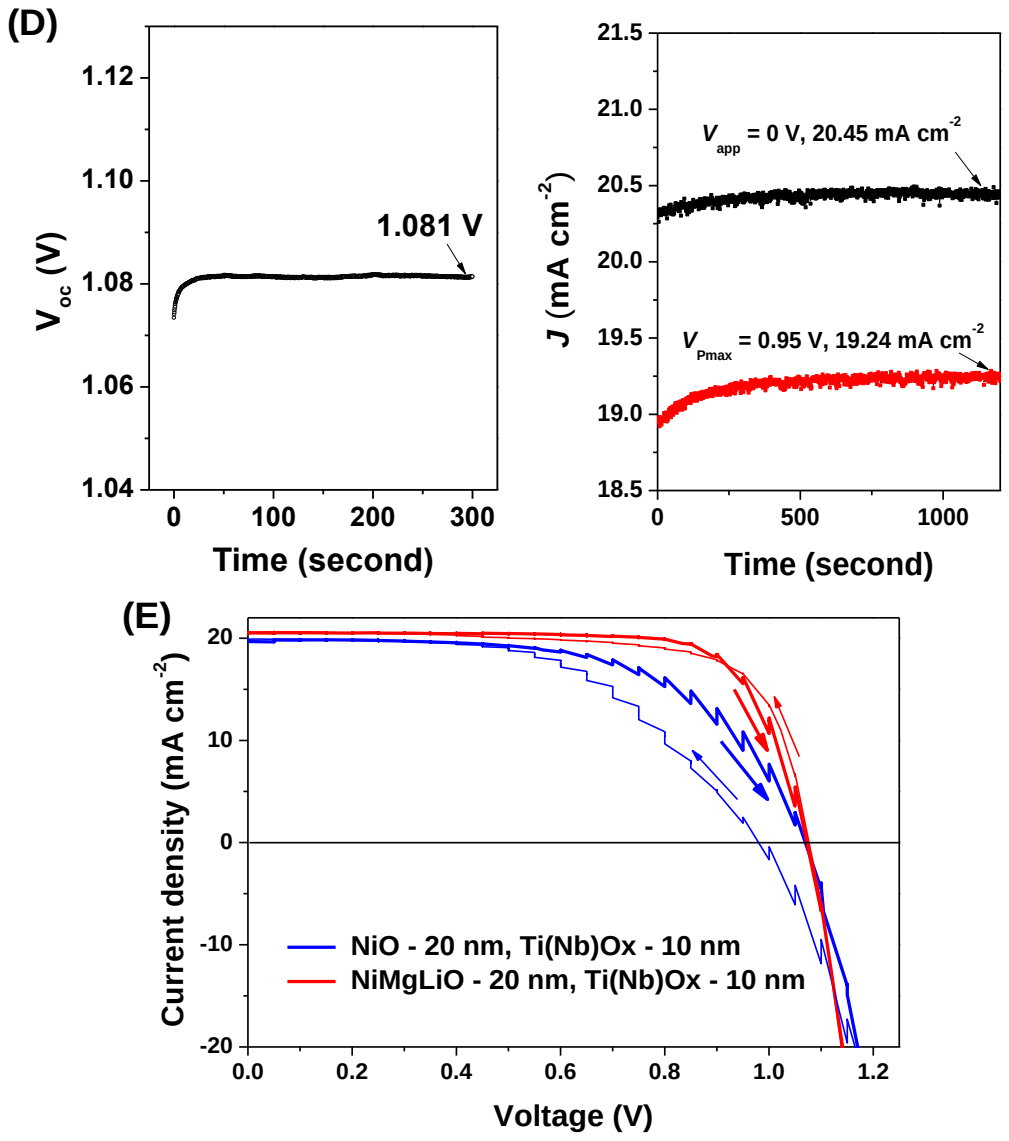


**Fig. S11**

(**A**-**B**) The *J*–*V* curves of the PSC (0.09 $cm^2$) with optimal charge extraction layers, obtained at different scan directions and step widths (5 mV–70 mV), with fixed delay time of 50 ms. (**B**) is the enlargement of (**A**) in bias region of 0.9–1.3 V. (**C**) A histogram comparing the difference in the *PCE*s obtained from scanning in the forward and reverse bias directions at the step width of 10 mV, based on a set of data measured with 40 different devices made from several batches. (**D**) The stead state $V_{oc}$, $J_{sc}$ and $P_{max}$ outputs of the solar cell in (**A**). The stable $P_{max}$ obtained at 0.95 V bias equals to 18.28% *PCE* of the solar cell, which is consistent with the *J*–*V* curves at small step widths (5–10 mV). (**E**) The stepwise *J*–*V* curves of the controlled solar cells with different interfacial conditions tested on an electrochemical workstation, with two opposite scan directions, step width = 50 mV and delay time = 5000 ms. The *J*–*V* hysteresis phenomenon will be enlarged at this scan condition. This result illustrates the effect of the charge carrier extraction layer composition on the hysteresis behavior of the PSC.

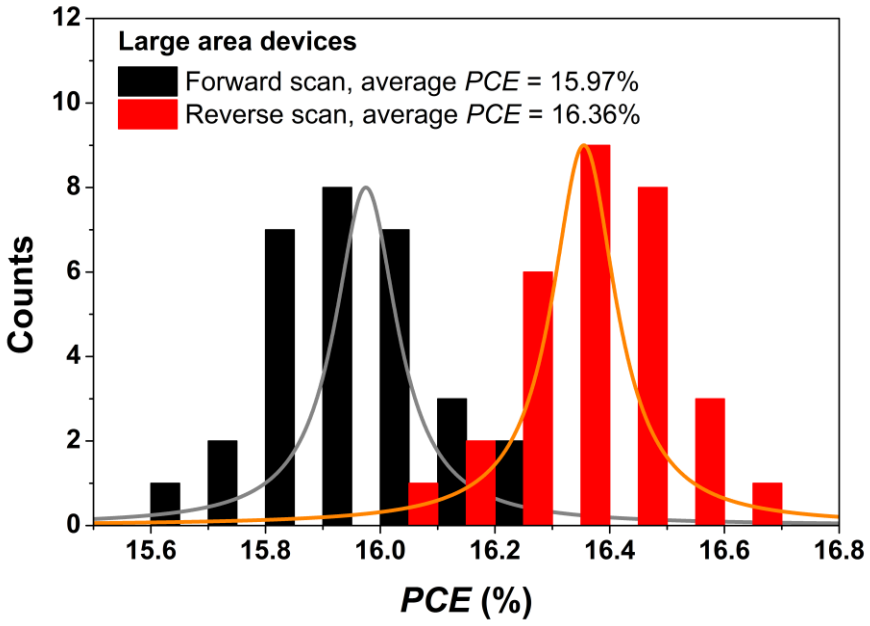


**Fig. S12**

A histogram comparing the difference in the *PCE*s of large area (1.02 $cm^2$) solar cells obtained from scanning in the forward and reverse bias directions, at the step width of 10 mV and delay time of 50 ms, based on a set of data measured with 30 different devices made from several batches. The average *PCE*s obtained from the two opposite scan directions are 15.97% and 16.36%, respectively.

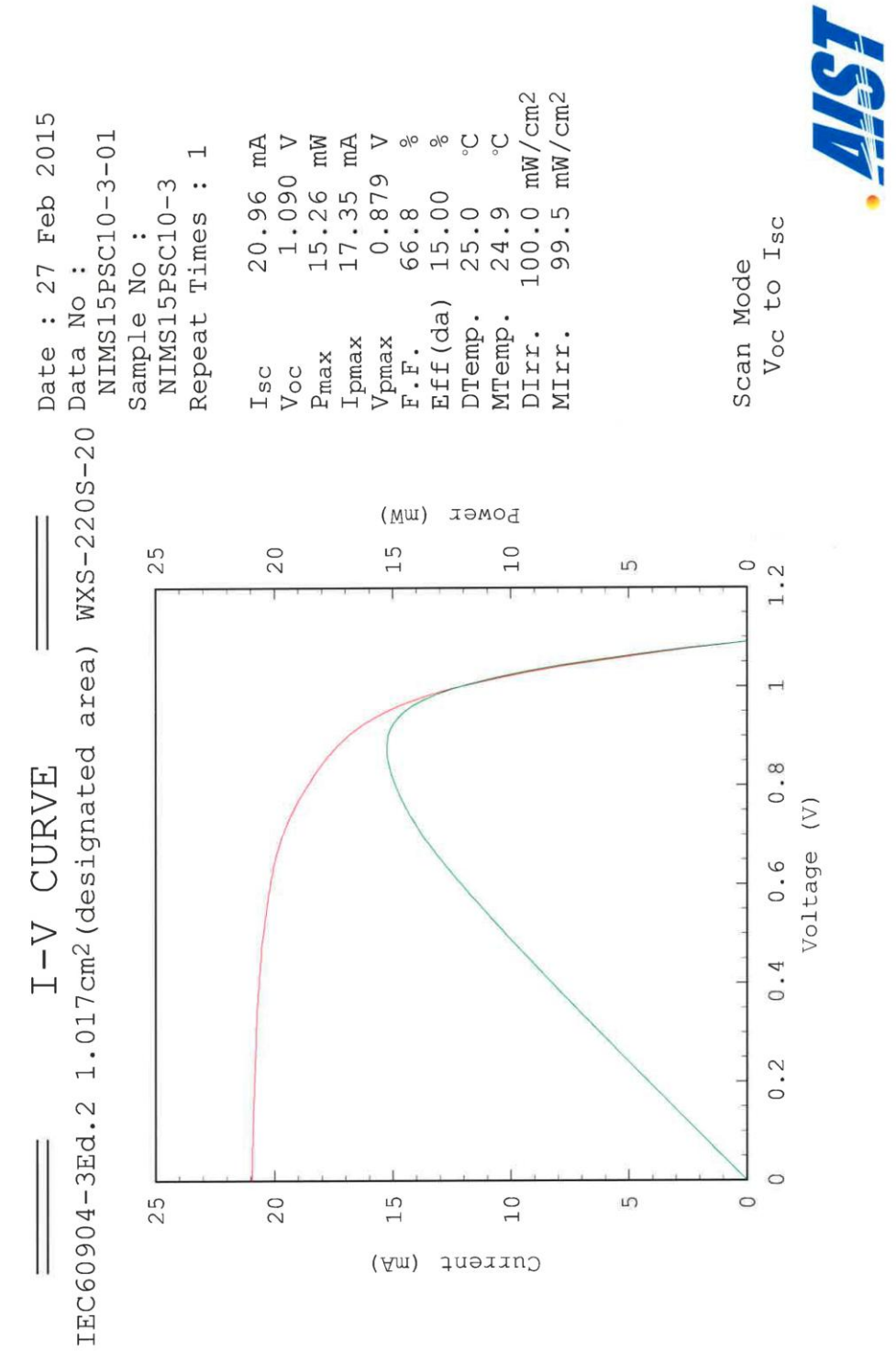


**Fig. S13**

The certified results from AIST with calibrated cell size of 1.017 $cm^2$.

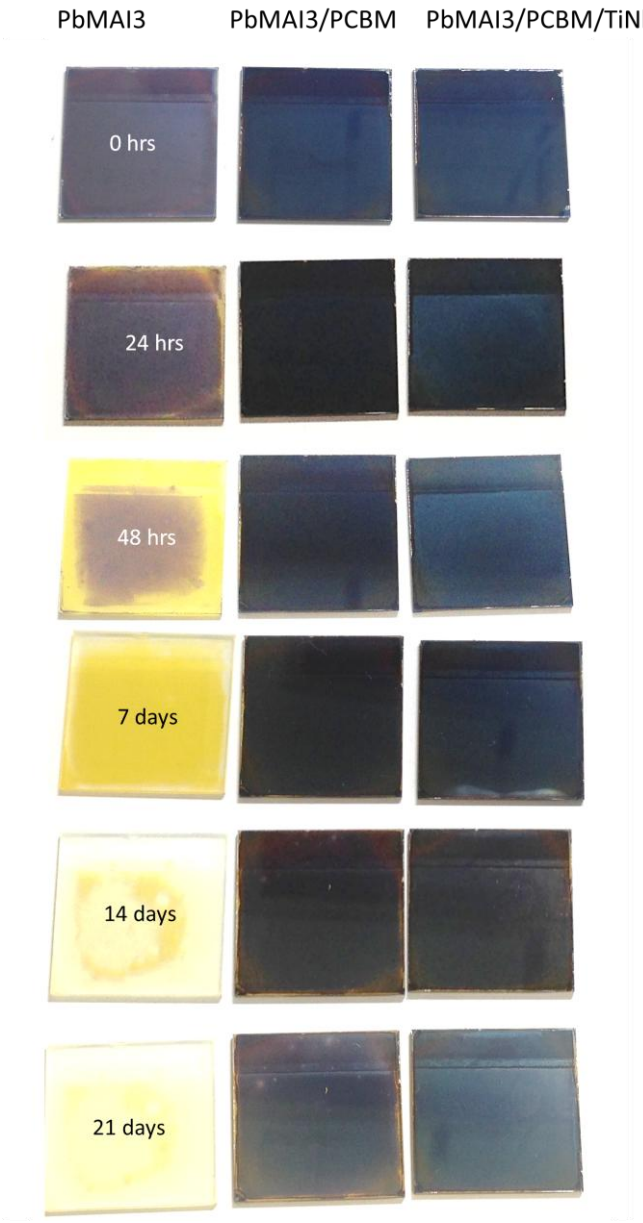


**Fig. S14**

Comparison of the perovskite layer degradation speeds (by monitoring color change from deep brown to light yellow and even transparent) without and with PCBM, Ti(Nb)$O_x$ protection layers. The films were kept in the ambient air and room light condition.

Bare perovskite film decomposed evidently after 24 hours, while PCBM and PCBM/Ti(Nb)$O_x$ covered perovskite films require at least two weeks to show first signs of decomposition. After 2–3 weeks, the different decomposition speeds between PCBM and PCBM/Ti(Nb)$O_x$ covered perovskite films are apparent from their color difference.

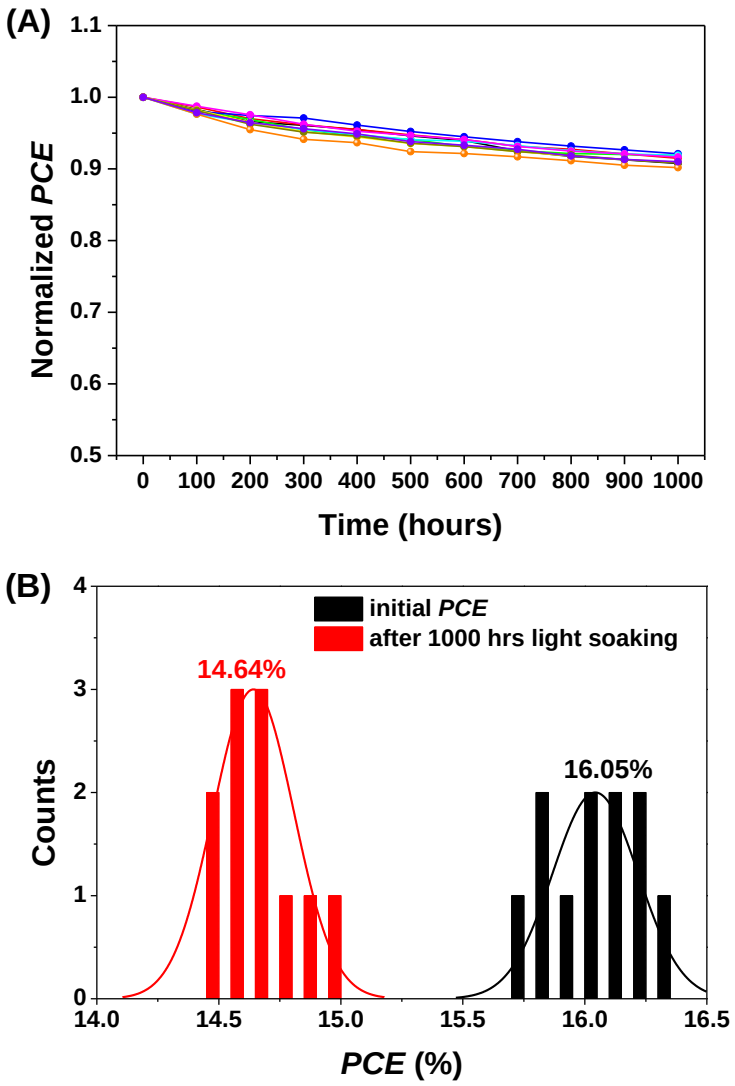


**Fig. S15**

A batch of 10 large cells (1.02 $cm^2$) with good sealing show similar *PCE*s degradation by <10%, after exposing to full sunlight from a solar simulator for 1000 hrs at short–circuit condition: (**A**) the normalized *PCE*s, (**B**) a histogram comparing the difference in the *PCE*s before and after 1000 hrs light soaking.

**Table S1.**

Summary on the landmark progresses on efficiency evolution of perovskite solar cells, the reported large size solar cells are included for better comparison to the present work.

| **Cell Structure** | ***PCE* (%)** | **Area ($cm^2$)** | **Hysteresis (Yes/No)** | **Certification (Yes/No)** | **Reference** |
|---|---|---|---|---|---|
| c-$TiO_2$/meso-$Al_2O_3$/$MAPbI_3$/Spiro-OMeTAD | 10.9 | 0.09 | Yes | No | *Science*, **2012**, 338, 643 |
| c-$TiO_2$/meso-$TiO_2$/$MAPbI_3$/Spiro-OMeTAD | 14.14 | 0.209 | Not stated | Yes, from Newport | *Nature*, **2013**, 499, 316 |
| c-$TiO_2$/$MAPbI_{3-x}Cl_x$/Spiro-OMeTAD | 15.4 | 0.09 | Yes | No | *Nature*, **2013**, 501, 395 |
| c-$TiO_2$/meso-$TiO_2$/$MAPb(I_{1-x}Br_x)_3$/PTAA | 16.2 | 0.16 | No | Yes, from Newport | *Nat. Mater.*, **2014**, 13, 897 |
| c-Y-$TiO_2$/$MAPbI_{3-x}Cl_x$/Spiro-OMeTAD | 19.3 | 0.1 | Yes | No | *Science*, **2014**, 345, 524 |
| c-$TiO_2$/meso-$TiO_2$/meso-$ZrO_2$/$(5\text{-}AVA)_x(MA)_{1-x}PbI_3$ /Carbon | 12.8 | 0.07 | No | Yes, from Newport | *Science*, **2014**, 345, 295 |
| c-$TiO_2$/meso-$TiO_2$/$(FAPbI_3)_{1-x}(MAPbBr_3)_x$/PTAA | 17.9 | 0. 09 | No | Yes, from Newport | *Nature*, **2015**, 517, 476 |
| c-$TiO_2$/meso-$TiO_2$/$(FAPbI_3)_{1-x}(MAPbBr_3)_x$/PTAA | 20.1 | 0.09 | No | Yes, from Newport | *Science*, **2015**, 348, 1234 |
| c-$TiO_2$/meso-$TiO_2$/$MAPbI_3$/Spiro-OMeTAD | 19.7 | 0.125 | Not stated | No | *JACS*, **2015**, 137, 869 |
| PEDOT: PSS/$MAPbI_{3-x}Cl_x$/PCBM | 18.0 | 0.035 | No | No | *Science*, **2015**, 347, 522 |
| c-$NiO_x$/$MAPbI_3$/PCBM/LiF | 17.3 | 0.04 | Not stated | No | *Adv. Mater.*, **2015**, 27, 4013 |
| c-$TiO_2$/meso-$TiO_2$/$MAPbI_3$/Spiro-OMeTAD | 12.6 | 1 | Not stated | No | *Nano Energy*, **2015**, 15, *670* |
| c-$TiO_2$/meso-$TiO_2$/$MAPbI_3$/Spiro-OMeTAD | 13.3<br>10.4<br>4.3 | 0.1<br>10.1<br>100 | Not stated | No | *J. Power. S.*, **2015**, 277, 286 |
| c-$TiO_2$/meso-$TiO_2$/$MAPbI_3$/Spiro-OMeTAD | 10.5 | 10.8 | Not stated | No | *ACS Nano*, **2015**, 9, 8420 |
| PEDOT: PSS/$MAPbI_3$/PCBM/$C_{60}$ | 10.9 | 0.95 | No | No | *Adv. Energy Mater.*, **2014**, 4, 1400345 |
| NiMgLiO/$MAPbI_3$/PCBM/Ti(Nb)$O_x$ | 15.0 | 1.017 | No | Yes, from AIST | *The present work* |

**Table S2.**

Photovoltaic performance metrics of the typical devices employing various combinations of charge carrier extraction layers with their *J*–*V* curves shown in Fig. 3A. The $R_{sh}$ and $R_s$ are obtained by linear fitting of the slopes for the *J*–*V* curves near the short–circuit condition and open–circuit condition, respectively.

| **Interfacial Conditions** | $J_{sc}$**(mA cm$^{-2}$)** | $V_{oc}$ **(V)** | ***FF*** | ***PCE* (%)** | $R_{sh}$ **(Ohm cm$^2$)** | $R_s$**(Ohm cm$^2$)** |
|---|---|---|---|---|---|---|
| $NiO/TiO_x$ | 18.7 | 1.036 | 0.640 | 12.4 | 1978 | 7.38 |
| $NiO/Ti(Nb)O_x$ | 19.2 | 1.047 | 0.731 | 14.7 | 3597 | 5.43 |
| $NiMgLiO/TiO_x$ | 20.0 | 1.074 | 0.768 | 16.5 | 2237 | 3.59 |
| $NiMgLiO/Ti(Nb)O_x$ | 20.4 | 1.083 | 0.827 | 18.3 | 5605 | 2.45 |

**Table S3.**

Efficiency parameters of the perovskite solar cell from *J–V* curves obtained at difference scan conditions. The corresponding *J–V* curves are shown in Fig. S11A.

| **Scan Direction** | **Step Width (mV)** | $J_{sc}$ **(mA cm$^{-2}$)** | $V_{oc}$ **(V)** | ***FF*** | ***PCE* (%)** |
|---|---|---|---|---|---|
| From $V_{oc}$ to $I_{sc}$ | 70 | 20.429 | 1.273 | 0.859 | 22.35 |
| | 20 | 20.427 | 1.167 | 0.836 | 19.92 |
| | 10 | 20.401 | 1.103 | 0.825 | 18.56 |
| | 5 | 20.387 | 1.096 | 0.823 | 18.40 |
| From $I_{sc}$ to $V_{oc}$ | 70 | 20.399 | 1.080 | 0.823 | 18.14 |
| | 20 | 20.431 | 1.084 | 0.823 | 18.23 |
| | 10 | 20.411 | 1.083 | 0.827 | 18.29 |
| | 5 | 20.418 | 1.085 | 0.830 | 18.39 |

## REFERENCES AND NOTES


1. G. Hodes, Perovskite-based solar cells. *Science* **342**, 317–318 (2013). Medline doi:10.1126/science.1245473

2. G. Xing, N. Mathews, S. Sun, S. S. Lim, Y. M. Lam, M. Grätzel, S. Mhaisalkar, T. C. Sum, Long-range balanced electron- and hole-transport lengths in organic-inorganic $CH_3NH_3PbI_3$. *Science* **342**, 344–347 (2013). Medline

3. Q. Dong, Y. Fang, Y. Shao, P. Mulligan, J. Qiu, L. Cao, J. Huang, Electron-hole diffusion lengths > 175 μm in solution-grown $CH_3NH_3PbI_3$ single crystals. *Science* **347**, 967–970 (2015). Medline doi:10.1126/science.aaa5760

4. M. Liu, M. B. Johnston, H. J. Snaith, Efficient planar heterojunction perovskite solar cells by vapour deposition. *Nature* **501**, 395–398 (2013). Medline doi:10.1038/nature12509

5. J. Burschka, N. Pellet, S. J. Moon, R. Humphry-Baker, P. Gao, M. K. Nazeeruddin, M. Grätzel, Sequential deposition as a route to high-performance perovskite-sensitized solar cells. *Nature* **499**, 316–319 (2013). Medline doi:10.1038/nature12340

6. N. J. Jeon, J. H. Noh, Y. C. Kim, W. S. Yang, S. Ryu, S. I. Seok, Solvent engineering for high-performance inorganic-organic hybrid perovskite solar cells. *Nat. Mater.* **13**, 897–903 (2014). Medline doi:10.1038/nmat4014

7. N. J. Jeon, J. H. Noh, W. S. Yang, Y. C. Kim, S. Ryu, J. Seo, S. I. Seok, Compositional engineering of perovskite materials for high-performance solar cells. *Nature* **517**, 476–480 (2015). Medline doi:10.1038/nature14133

8. W. S. Yang, J. H. Noh, N. J. Jeon, Y. C. Kim, S. Ryu, J. Seo, S. I. Seok, High-performance photovoltaic perovskite layers fabricated through intramolecular exchange. *Science* **348**, 1234–1237 (2015). Medline doi:10.1126/science.aaa9272

9. J. H. Heo, H. J. Han, D. Kim, T. K. Ahn, S. H. Im, Stable semi-transparent $CH_3NH_3PbI_3$ planar sandwich solar cells. *Energy Environ. Sci.* **8**, 1602–1608 (2015).

10. W. Nie, H. Tsai, R. Asadpour, J. C. Blancon, A. J. Neukirch, G. Gupta, J. J. Crochet, M. Chhowalla, S. Tretiak, M. A. Alam, H. L. Wang, A. D. Mohite, High-efficiency solution-processed perovskite solar cells with millimeter-scale grains. *Science* **347**, 522–525 (2015). Medline doi:10.1126/science.aaa0472

11. J. H. Park, J. Seo, S. Park, S. S. Shin, Y. C. Kim, N. J. Jeon, H. W. Shin, T. K. Ahn, J. H. Noh, S. C. Yoon, C. S. Hwang, S. I. Seok, Efficient $CH_3NH_3PbI_3$ perovskite solar cells employing nanostructured p-type NiO electrode formed by a pulsed laser deposition. *Adv. Mater.* **27**, 4013–4019 (2015). Medline doi:10.1002/adma.201500523

12. A. Mei, X. Li, L. Liu, Z. Ku, T. Liu, Y. Rong, M. Xu, M. Hu, J. Chen, Y. Yang, M. Grätzel, H. Han, A hole-conductor–free, fully printable mesoscopic perovskite solar cell with high stability. *Science* **345**, 295–298 (2014). Medline

13. X. Li, M. Tschumi, H. Han, S. S. Babkair, R. A. Alzubaydi, A. A. Ansari, S. S. Habib, M. K. Nazeeruddin, S. M. Zakeeruddin, M. Grätzel, Outdoor performance and stability under elevated temperatures and long-term light soaking of triple-layer mesoporous perovskite photovoltaics. *Energy Technol.* **3**, 551–555 (2015). doi:10.1002/ente.201500045

14. Materials and methods are available as supplementary materials on *Science* Online.

15. M. A. Green, K. Emery, Y. Hishikawa, W. Warta, E. D. Dunlop, Solar cell efficiency tables (Version 45). *Prog. Photovolt. Res. Appl.* **23**, 1–9 (2015). doi:10.1002/pip.2573

16. M. C. Beard, J. M. Luther, A. J. Nozik, The promise and challenge of nanostructured solar cells. *Nat. Nanotechnol.* **9**, 951–954 (2014). Medline doi:10.1038/nnano.2014.292

17. E. Zimmermann, P. Ehrenreich, T. Pfadler, J. A. Dorman, J. Weickert, L. Schmidt-Mende, Erroneous efficiency reports harm organic solar cell research. *Nat. Photonics* **8**, 669–672 (2014). doi:10.1038/nphoton.2014.210

18. K. D. G. I. Jayawardena, L. J. Rozanski, C. A. Mills, S. R. P. Silva, The true status of solar cell technology. *Nat. Photonics* **9**, 207–208 (2015). doi:10.1038/nphoton.2015.45

19. Bringing solar cell efficiencies into the light. *Nat. Nanotechnol.* **9**, 657 (2014).

20. O. Malinkiewicz, C. Roldán-Carmona, A. Soriano, E. Bandiello, L. Camacho, M. K. Nazeeruddin, H. J. Bolink, Metal-oxide-free methylammonium lead iodide perovskite-based solar cells: The influence of organic charge transport layers. *Adv. Energy Mater.* **4**, 1400345 (2014). doi:10.1002/aenm.201400345

21. Z. Yang, B. Cai, B. Zhou, T. Yao, W. Yu, S. F. Liu, W.-H. Zhang, C. Li, An up-scalable approach to $CH_3NH_3PbI_3$ compact films for high-performance perovskite solar cells. *Nano Energy* **15**, 670–678 (2015). doi:10.1016/j.nanoen.2015.05.027

22. M. Grätzel, The light and shade of perovskite solar cells. *Nat. Mater.* **13**, 838–842 (2014). Medline doi:10.1038/nmat4065

23. M. Gunther, "Meteoritic rise of perovskite solar cells under scrutiny over efficiencies," *Chemistry World*, 2 March 2015; www.rsc.org/chemistryworld/2015/02/meteoritic-rise-perovskite-solar-cells-under-scrutiny-over-efficiencies.

24. H. Zhou, Q. Chen, G. Li, S. Luo, T. B. Song, H. S. Duan, Z. Hong, J. You, Y. Liu, Y. Yang, Interface engineering of highly efficient perovskite solar cells. *Science* **345**, 542–546 (2014). Medline doi:10.1126/science.1254050

25. O. Malinkiewicz, A. Yella, Y. H. Lee, G. M. Espallargas, M. Graetzel, M. K. Nazeeruddin, H. J. Bolink, Perovskite solar cells employing organic charge-transport layers. *Nat. Photonics* **8**, 128–132 (2014). doi:10.1038/nphoton.2013.341

26. Q. Lin, A. Armin, R. C. R. Nagiri, P. L. Burn, P. Meredith, Electro-optics of perovskite solar cells. *Nat. Photonics* **9**, 106–112 (2015). doi:10.1038/nphoton.2014.284

27. A. G. Aberle, Surface passivation of crystalline silicon solar cells: A review. *Prog. Photovolt. Res. Appl.* **8**, 473–487 (2000). doi:10.1002/1099-159X(200009/10)8:5<473::AID-PIP337>3.0.CO;2-D

28. M. A. Green, K. Emery, Y. Hishikawa, W. Warta, E. D. Dunlop, Solar cell efficiency tables (version 46). *Prog. Photovolt. Res. Appl.* **23**, 805–812 (2015). doi:10.1002/pip.2637

29. M. A. Wittenauer, L. L. Van Zandt, Surface conduction versus bulk conduction in pure stoichiometric NiO crystals. *Philos. Mag. B* **46**, 659–667 (1982). doi:10.1080/01418638208223551

30. J. H. Kim, P. W. Liang, S. T. Williams, N. Cho, C. C. Chueh, M. S. Glaz, D. S. Ginger, A. K. Jen, High-performance and environmentally stable planar heterojunction perovskite solar cells based on a solution-processed copper-doped nickel oxide hole-transporting layer. *Adv. Mater.* **27**, 695–701 (2015). Medline doi:10.1002/adma.201404189

31. Z. Zhu, Y. Bai, T. Zhang, Z. Liu, X. Long, Z. Wei, Z. Wang, L. Zhang, J. Wang, F. Yan, S. Yang, High-performance hole-extraction layer of sol–gel-processed $NiO_x$ nanocrystals for inverted planar perovskite solar cells. *Angew. Chem. Int. Ed.* **53**, 12571–12575 (2014).

32. C. Wu, C. Yang, Effect of annealing temperature on the characteristics of the modified spray deposited Li-doped NiO films and their applications in transparent heterojunction diode. *Sol. Energy Mater. Sol. Cells* **132**, 492–498 (2015). doi:10.1016/j.solmat.2014.09.017

33. Y. H. Kim, C. Sachse, M. L. Machala, C. May, L. Müller-Meskamp, K. Leo, Highly conductive PEDOT:PSS electrode with optimized solvent and thermal post-treatment for ITO-free organic solar cells. *Adv. Funct. Mater.* **21**, 1076–1081 (2011). doi:10.1002/adfm.201002290

34. W. Chen, Y. Wu, J. Liu, C. Qin, X. Yang, A. Islam, Y.-B. Cheng, L. Han, Hybrid interfacial layer leads to solid performance improvement of inverted perovskite solar cells. *Energy Environ. Sci.* **8**, 629–640 (2015).

35. N. Alidoust, M. C. Toroker, J. A. Keith, E. A. Carter, Significant reduction in NiO band gap upon formation of $Li_xNi_{1-x}O$ alloys: Applications to solar energy conversion. *ChemSusChem* **7**, 195–201 (2014). Medline doi:10.1002/cssc.201300595

36. U. S. Joshi, Y. Matsumoto, K. Itaka, M. Sumiya, H. Koinuma, Combinatorial synthesis of Li-doped NiO thin films and their transparent conducting properties. *Appl. Surf. Sci.* **252**, 2524–2528 (2006). doi:10.1016/j.apsusc.2005.03.239

37. Z. Huang, X. Zeng, H. Wang, W. Zhang, Y. Li, M. Wang, Y.-B. Cheng, W. Chen, Enhanced performance of p-type dye sensitized solar cells based on mesoporous $Ni_{1-x}$ $Mg_xO$ ternary oxide films. *RSC Adv.* **4**, 60670–60674 (2014). doi:10.1039/C4RA09727K

38. J. Deng, M. Mortazavi, N. V. Medhekar, J. Zhe Liu, Band engineering of $Ni_{1-x}Mg_xO$ alloys for photocathodes of high efficiency dye-sensitized solar cells. *J. Appl. Phys.* **112**, 123703 (2012). doi:10.1063/1.4769210

39. K. Lee, J. Y. Kim, S. H. Park, S. H. Kim, S. Cho, A. J. Heeger, Air-stable polymer electronic devices. *Adv. Mater.* **19**, 2445–2449 (2007). doi:10.1002/adma.200602653

40. T. Kuwabara, T. Nakayama, K. Uozumi, T. Yamaguchi, K. Takahashi, Highly durable inverted-type organic solar cell using amorphous titanium oxide as electron collection electrode inserted between ITO and organic layer. *Sol. Energy Mater. Sol. Cells* **92**, 1476–1482 (2008). doi:10.1016/j.solmat.2008.06.012

41. T. Kuwabara, H. Sugiyama, T. Yamaguchi, K. Takahashi, Inverted type bulk-heterojunction organic solar cell using electrodeposited titanium oxide thin films as electron collector electrode. *Thin Solid Films* **517**, 3766–3769 (2009). doi:10.1016/j.tsf.2008.12.039

42. K. Wojciechowski, M. Saliba, T. Leijtens, A. Abate, H. J. Snaith, Sub-150 °C processed meso-superstructured perovskite solar cells with enhanced efficiency. *Energy Environ. Sci.* **7**, 1142–1147 (2014).

43. Y. Furubayashi, T. Hitosugi, Y. Yamamoto, K. Inaba, G. Kinoda, Y. Hirose, T. Shimada, T. Hasegawa, A transparent metal: Nb-doped anatase $TiO_2$. *Appl. Phys. Lett.* **86**, 252101–252103 (2005). doi:10.1063/1.1949728

44. S. Braun, W. R. Salaneck, M. Fahlman, Energy-level alignment at organic/metal and organic/organic interfaces. *Adv. Mater.* **21**, 1450–1472 (2009). doi:10.1002/adma.200802893

45. J. H. Heo, D. H. Song, H. J. Han, S. Y. Kim, J. H. Kim, D. Kim, H. W. Shin, T. K. Ahn, C. Wolf, T. W. Lee, S. H. Im, Planar $CH_3NH_3PbI_3$ perovskite solar cells with constant 17.2% average power conversion efficiency irrespective of the scan rate. *Adv. Mater.* **27**, 3424–3430 (2015). Medline doi:10.1002/adma.201500048

46. X. Liu, H. Yu, L. Yan, Q. Dong, Q. Wan, Y. Zhou, B. Song, Y. Li, Triple cathode buffer layers composed of PCBM, $C_{60}$, and LiF for high-performance planar perovskite solar cells. *ACS Appl. Mater. Interfaces* **7**, 6230–6237 (2015). Medline doi:10.1021/acsami.5b00468

47. J. Liu, Y. Shirai, X. Yang, Y. Yue, W. Chen, Y. Wu, A. Islam, L. Han, High-quality mixed-organic-cation perovskites from a phase-pure non-stoichiometric intermediate $(FAI)_{1-x}$-$PbI_2$ for solar cells. *Adv. Mater.* **27**, 4918–4923 (2015). Medline doi:10.1002/adma.201501489

48. P. Puspharajah, S. Radhakrishna, A. K. Arof, Transparent conducting lithium-doped nickel oxide thin films by spray pyrolysis technique. *J. Mater. Sci.* **32**, 3001–3006 (1997). doi:10.1023/A:1018657424566

49. T. Dutta, P. Gupta, A. Gupta, J. Narayan, Effect of Li doping in NiO thin films on its transparent and conducting properties and its application in heteroepitaxial p-n junctions. *J. Appl. Phys.* **108**, 083715 (2010). doi:10.1063/1.3499276

50. T. Moehl, J. H. Im, Y. H. Lee, K. Domanski, F. Giordano, S. M. Zakeeruddin, M. I. Dar, L. P. Heiniger, M. K. Nazeeruddin, N. G. Park, M. Grätzel, Strong photocurrent amplification in perovskite solar cells with a porous TiO2 blocking layer under reverse bias. *J. Phys. Chem. Lett.* **5**, 3931–3936 (2014). Medline